



Fermi-arc supercurrent oscillations in Dirac semimetal Josephson junctions

Cai-Zhen Li^{1,2,7}, An-Qi Wang^{3,7}, Chuan Li⁴, Wen-Zhuang Zheng¹, Alexander Brinkman⁴, Da-Peng Yu² & Zhi-Min Liao^{1,5,6}

One prominent hallmark of topological semimetals is the existence of unusual topological surface states known as Fermi arcs. Nevertheless, the Fermi-arc superconductivity remains elusive. Here, we report the critical current oscillations from surface Fermi arcs in Nb-Dirac semimetal Cd₃As₂-Nb Josephson junctions. The supercurrent from bulk states are suppressed under an in-plane magnetic field -0.1 T, while the supercurrent from the topological surface states survives up to 0.5 T. Contrary to the minimum normal-state conductance, the Fermi-arc carried supercurrent shows a maximum critical value near the Dirac point, which is consistent with the fact that the Fermi arcs have maximum density of state at the Dirac point. Moreover, the critical current exhibits periodic oscillations with a parallel magnetic field, which is well understood by considering the in-plane orbital effect from the surface states. Our results suggest the Dirac semimetal combined with superconductivity should be promising for topological quantum devices.

¹State Key Laboratory for Mesoscopic Physics and Frontiers Science Center for Nano-optoelectronics, School of Physics, Peking University, Beijing 100871, China. ²Shenzhen Institute for Quantum Science and Engineering and Department of Physics, Southern University of Science and Technology, Shenzhen 518055, China. ³Academy for Advanced Interdisciplinary Studies, Peking University, Beijing 100871, China. ⁴MESA+ Institute for Nanotechnology, University of Twente, 7500 AE Enschede, The Netherlands. ⁵Beijing Key Laboratory of Quantum Devices, Peking University, Beijing 100871, China. ⁶Collaborative Innovation Center of Quantum Matter, Peking University, Beijing 100871, China. ⁷These authors contributed equally: Cai-Zhen Li, An-Qi Wang. ✉email: chuan.li@utwente.nl; liaozm@pku.edu.cn

Materials with topological surface states have become one of the most intensive fields of condensed matter research in past years^{1–3}. Among the various topological materials, the topological semimetal has sparked substantial interest due to its gapless Weyl/Dirac cones and unique surface Fermi arcs^{3–5}. With nontrivial Fermi-arc surface states^{5–9}, the Dirac semimetal Cd₃As₂ has demonstrated exotic quantum transport properties of these surface states, such as π Aharonov–Bohm effect^{9,10}, Fermi-arc-mediated Weyl orbital transport^{11,12}, and quantum Hall effect from topologically protected Fermi arcs^{13–17}. Besides the transport research in its normal phase, efforts have recently been made to couple the Fermi-arc surface states to a superconductor with the expectation of Majorana fermions^{18–21}. Such proximitized superconductivity has been observed in Cd₃As₂, including surface carried Josephson supercurrent²², π and 4π Josephson effects^{23,24}. For the potential control of Majorana fermions and real-life application of topological quantum computation, it is of great necessity to establish a good manipulation over the superconducting Fermi-arc states.

Here, we report the magnetic field and gate modulation of the Fermi-arc superconductivity in Nb–Cd₃As₂–Nb Josephson junctions. Without magnetic field, the supercurrent is carried by both bulk and surface states. With increasing an in-plane magnetic field, the bulk-carried supercurrent is strongly suppressed and the Fermi-arc surface states become manifest. In the surface state dominant regime, the critical supercurrent shows a maximum value near the Dirac point, consistent with the fact that the Fermi arcs have the maximum density of states at the Dirac point. The maximum critical supercurrent at Dirac point in 3D Dirac semimetal is different from the case of 2D Dirac states in topological insulators and graphene. Furthermore, the Fermi-arc supercurrent shows periodic oscillations with in-plane parallel magnetic field, which is attributed to the in-plane field orbital interference of the surface Fermi arcs. Such magnetic field and gate modulation of superconducting Fermi arcs open up a new avenue for the manipulation of Majorana fermions, which might be significant to the topological quantum computation.

Results

Andreev reflections in the Dirac semimetal Josephson junction.

The Josephson junctions consist of Cd₃As₂ nanoplates and superconducting Nb electrodes (Fig. 1a). The Cd₃As₂ nanoplates are of high crystalline quality with (112) oriented surfaces (Supplementary Fig. 1). Individual Cd₃As₂ nanoplates were transferred into a silicon substrate with a SiO₂ layer (285 nm), which serves as the back gate. The separation length L between the two

Nb electrodes is about 300 nm for the measured junction presented in the main text. The average width W of the nanoplate is 5 μm . The flake thickness t is about 80 nm. Electrical transport measurements were performed in a dilution refrigerator with a base temperature of 12 mK.

Figure 1b shows the differential resistance (dV/dI) as a function of current bias I_{dc} and gate voltage (V_g). A gate tunable nondissipative supercurrent is observed. As tuning V_g from 60 to -60 V, the critical current I_c first increases and reaches a maximum value of 1 μA at around $V_g = 20$ V, and then decreases rapidly to about 50 nA when $V_g < -50$ V. The strong suppression of I_c at negative V_g is due to the low hole mobility of bulk states in Cd₃As₂ (ref. 25). The behavior of I_c peak at $V_g = 20$ V is resulted from the coexistence of bulk and surface states as demonstrated later. In Fig. 1c, we show the dV/dI as a function of the bias voltage (V_{dc}) between two superconducting electrodes at different gate voltages. A series of dips in dV/dI spectra at $V_n = 2\Delta/ne$ ($n = 1, 2, \dots$) are attributed to the multiple Andreev reflections. The induced superconducting gap is estimated to be 0.9 meV, which is smaller than the gap value of the Nb layers (1.4 meV).

Supercurrent oscillations under in-plane magnetic field.

When an in-plane magnetic field \mathbf{B} is applied parallel to the current direction, the critical current I_c first shows a rapid decay, and then oscillates periodically as a function of \mathbf{B} . Figure 2a shows a typical spectrum of dV/dI as a function of \mathbf{B} and I_{dc} . The I_c decreases from 1.1 μA to ~ 65 nA as increasing \mathbf{B} from 0 to 70 mT. The I_c then exhibits an oscillating behavior until 0.5 T (Fig. 2b).

The critical current of a diffusive thin film is expected to decrease monotonically in a parallel magnetic field with $I_c(\mathbf{B}) \approx I_c(0)e^{-B^2/2\sigma^2}$, like a Gaussian function²⁶, where σ is the decay coefficient. A Gaussian fit can well describe the I_c trends under low field, but obviously fails in the case of high field, where I_c is suppressed with a much lower rate (Fig. 2c). A kink behavior is clearly observed near 0.1 T, which separates the two different drop rates of I_c under low and high magnetic fields. This implies that two channels (bulk and surface) coexist and respond differently to magnetic field. Under zero magnetic field, there is an unavoidable coexistence of bulk and surface states due to the highly conductive bulk and large surface-to-volume ratio in nanostructured Cd₃As₂. When applying a magnetic field, the supercurrent from the bulk states is strongly suppressed, while the supercurrent from surface states can still survive up to 0.5 T benefiting from the topological nature and protection from backscattering. Thus the surface states are responsible for the supercurrent under high magnetic field that decays with a much lower rate. After subtracting the decay

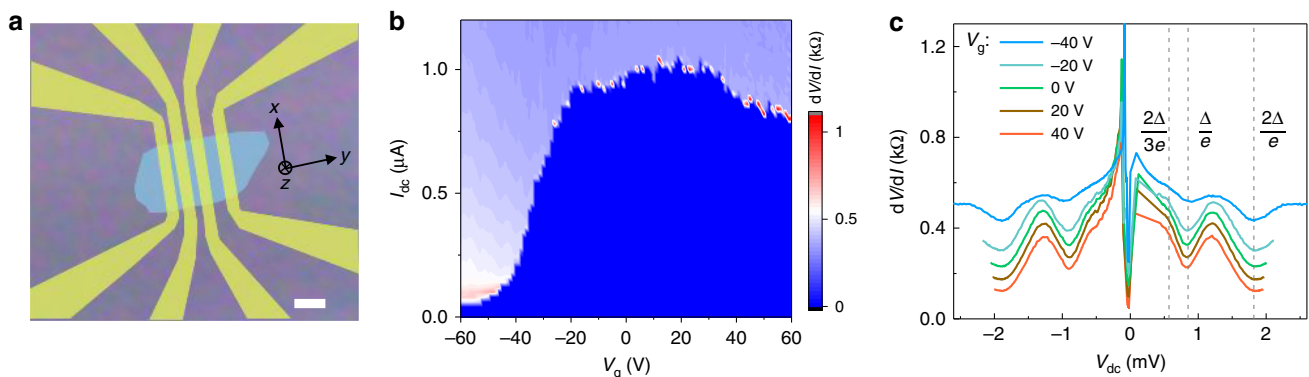


Fig. 1 Josephson effect in a Nb–Cd₃As₂–Nb junction. **a** Optical image of the Nb–Cd₃As₂ nanoplate–Nb Josephson junctions. Scale bar, 2 μm . **b** The color-scale differential resistance dV/dI as a function of gate voltage V_g and d.c. bias current I_{dc} . **c** The dV/dI versus source-drain voltage V_{dc} across the junction, showing the multiple Andreev reflections.

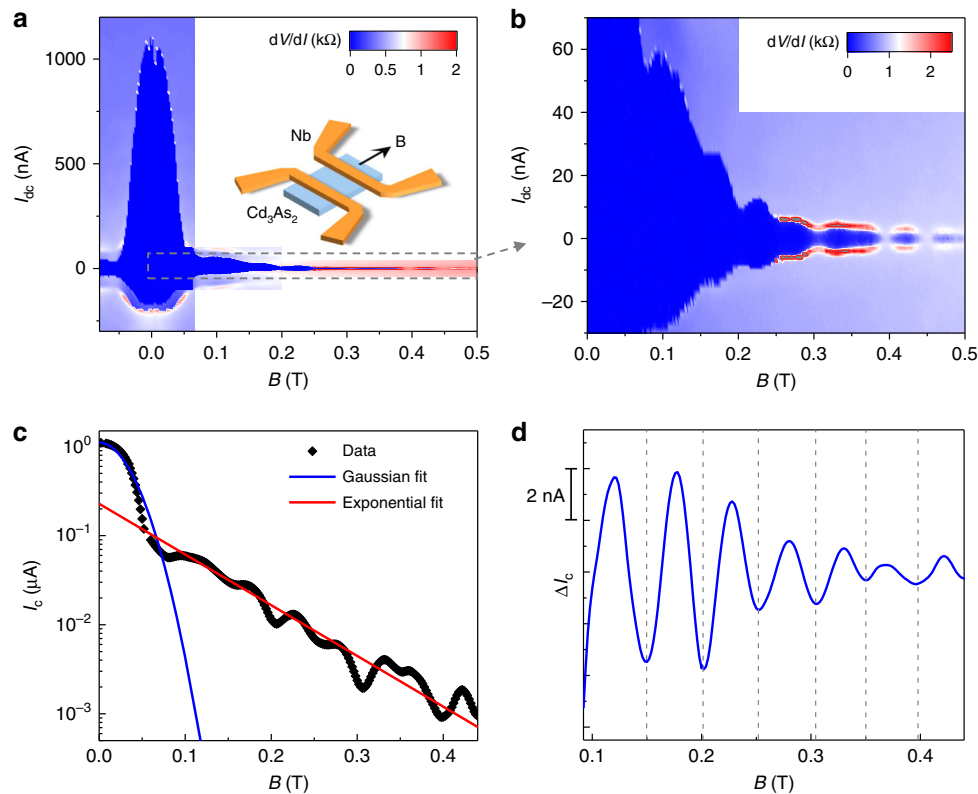


Fig. 2 The supercurrent oscillations under parallel magnetic field at $V_g = 0$ V. **a** The dV/dI as a function of magnetic field \mathbf{B} and I_{dc} . The I_{dc} is swept from negative to positive. The applied excitation current $I_{ac} = 0.5$ nA. Inset: Schematic of the magnetic field direction on the junction. **b** The enlarged dV/dI map of the gray dotted box in **a**. Periodic supercurrent oscillations with multiple nodes are observed. **c** The magnetic field dependence of I_c with a semilog coordinate. The Gaussian fitting (blue curve) well models the decay trend of I_c at low \mathbf{B} , and an exponential decay (red line) fits better the data for $\mathbf{B} > 0.1$ T. **d** The extracted ΔI_c by subtracting a smooth background as a function of \mathbf{B} . A period of $\Delta \mathbf{B} = 0.05$ T is obtained from the oscillations.

background under high magnetic field, the plot of ΔI_c with \mathbf{B} demonstrates periodic oscillations with a period of $\Delta \mathbf{B} \sim 0.05$ T, as shown in Fig. 2d.

Gate tuned critical supercurrent carried by Fermi arcs. The I_c oscillations are further investigated by tuning the Fermi level of the Cd_3As_2 nanoplate. Figure 3a, b show a series of dV/dI as a function of \mathbf{B} and I_{dc} at different values of V_g . As varying V_g , the oscillation period $\Delta \mathbf{B}$ remains unchanged with discernible oscillating nodes, as marked by the uniformly spaced dashed lines in Fig. 3c. The constant period as a function of the gate voltage indicates that the critical current oscillations are insensitive to the carrier density. Figure 3d shows the comparison between I_c and normal-state conductance G_N (measured at $I_{dc} = 100$ nA) under $\mathbf{B} = 0.1$ T. Near the Dirac point, the G_N reaches a minimum, while I_c unexpectedly acquires a maximum value, indicating that the dominant conduction channels for the superconducting and normal states are different.

The coexistence of bulk and surface states is reflected by the I_c evolution with magnetic field (Fig. 3e). Under zero field, the I_c shows a rapid increase as tuning the Fermi level from the hole conduction region to the Dirac point, while increases slightly with further increasing gate voltage to 20 V, and then shows a downward trend for $V_g > 20$ V. Considering the screening of gate electric field at large V_g , the inhomogeneous carrier distribution may break the Andreev pairs and reduce the I_c . Since the bulk pairing can be greatly suppressed by magnetic field, the I_c is significantly reduced under 0.1 T, and a I_c peak appears near the Dirac point. Further increasing magnetic field to 0.18 and 0.23 T, the position of the I_c peak keeps unchanged at around $V_g = -10$ V, indicating a fully

surface state dominant regime. In Cd_3As_2 , the surface states are in the form of Fermi arcs, which connect the projection of two bulk Dirac points on the surface. As tuning the bulk Fermi level close to the Dirac point, the proportion of Fermi arc would acquire a maximum value (Fig. 3f). Thus, in a surface dominant regime, the Fermi arc carried supercurrent would acquire a maximum value near the Dirac point. Moreover, at the Dirac point, the density of state of bulk is minimum, and thus the less scattering from the bulk state also facilitates the Fermi-arc supercurrent²². The Fermi-arc supercurrent survives at higher magnetic field, which is attributed to the topological protection and long phase coherence length of the Andreev pair states.

The superconducting state transition and its gate dependence are further studied by the measurement of dV/dI as a function of \mathbf{B} and V_g with $I_{ac} = 1$ nA and without applying I_{dc} . Figure 4 shows that the superconducting state also exhibits an oscillating pattern with increasing \mathbf{B} . In the whole range of magnetic field upto 0.5 T, six distinct superconducting regions are clearly separated, as marked in Fig. 4a by the red dashed lines. To highlight the periodically reentrant behavior of the superconducting state, the dV/dI as a function of \mathbf{B} at different V_g is plotted in Fig. 4b. The junction transforms from the superconducting state to normal state at around $\mathbf{B} \sim 0.19$ T. With further increasing \mathbf{B} , the system then reenters into the superconducting state. The dV/dI peaks are nearly periodic in \mathbf{B} with a period of around 0.055 T, which is consistent with the I_c oscillation period (0.05 T). The superconducting state always exists until 0.19 T (Fig. 4a), which is mainly due to the fact that the bulk states can carry supercurrent in low field and is consistent with the nonzero critical current at the I_c oscillation nodes in low field (Fig. 2b).

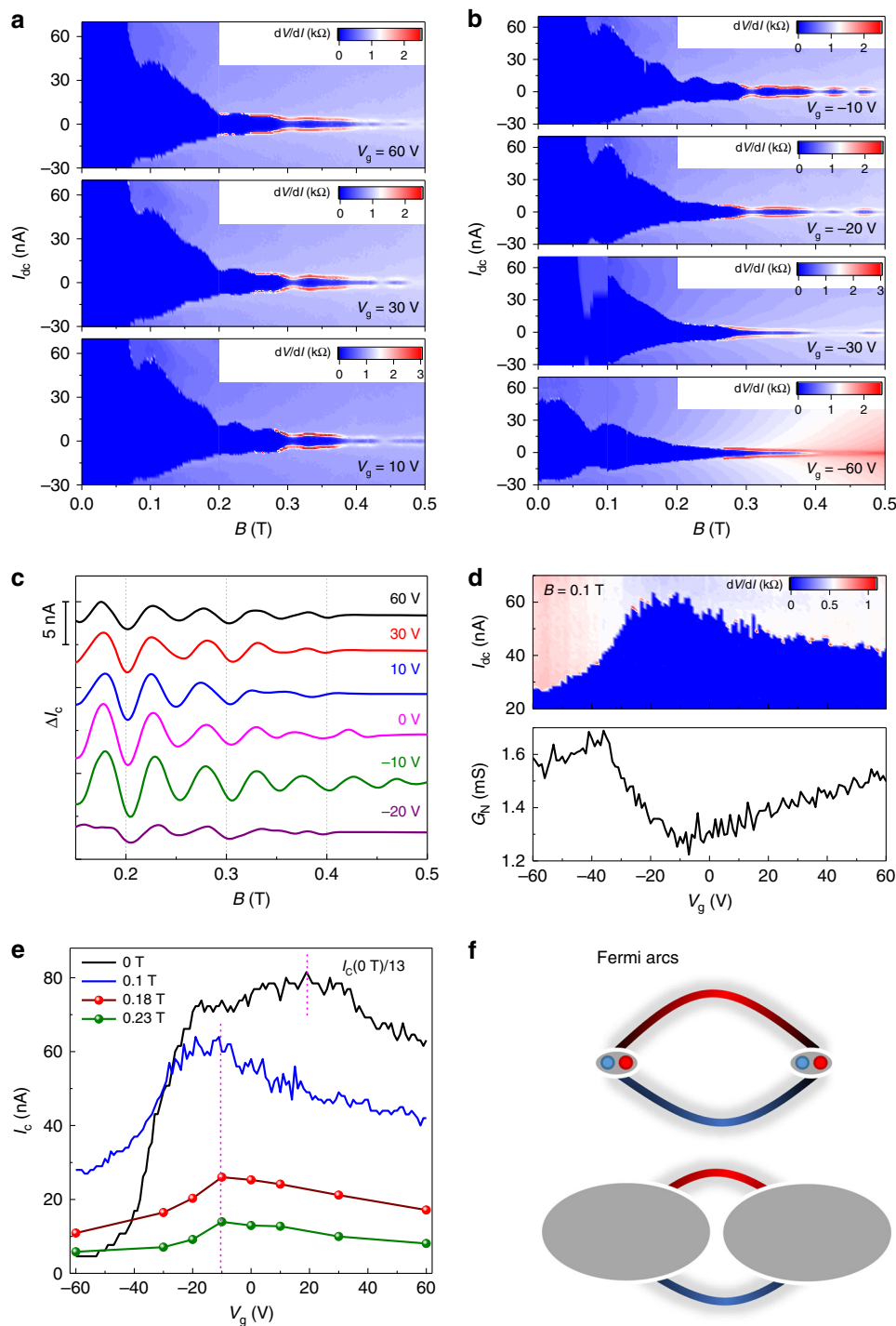


Fig. 3 Gate dependence of supercurrent oscillations. **a, b** Color-scale plot of dV/dI as a function of B and I_{dc} at different V_g as denoted. **c** The extracted ΔI_c versus B at different V_g . The curves have been shifted for clarity. **d** The comparison between critical current I_c and normal-state conductance G_N as a function of V_g , measured at $B = 0.1$ T. **e** $I_c(V_g)$ evolutions under different magnetic fields. The $I_c(0\text{T})$ divided by 13 is shown in the figure. The $I_c(0.18\text{T})$ and $I_c(0.23\text{T})$ are extracted from the $I_c(B)$ peaks of the first and second oscillation lobes in **c**, respectively. **f** The Fermi arcs for the Fermi level (up panel) close to and (bottom panel) away from Dirac point. The bulk Dirac points are projected on (112) crystal plane of the Cd_3As_2 nanoplate.

Discussion

From the above results, we can conclude that the supercurrent is carried mainly by the Fermi-arc surface states of the nanoplate under high magnetic field. Next we would like to discuss the possible mechanisms of the supercurrent oscillations with magnetic field. Recent studies show that, in certain materials, the mechanism of finite momentum Cooper pairing can give rise to extra superconducting coherence and spatially oscillating parameter when

subjected to in-plane magnetic exchange fields^{27–29}. Critical current oscillations in superconductor–ferromagnet–superconductor junctions have provided evidences for both nonzero pairing momentum and $0-\pi$ transition^{30–32}. More recently, quantum oscillations arising from in-plane Zeeman field induced finite momentum pairing have been demonstrated in Josephson systems of a Bi nanowire³³, topological insulators^{34–36}, and a $\text{Bi}_{0.97}\text{Sb}_{0.03}$ topological semimetal^{37,38}.

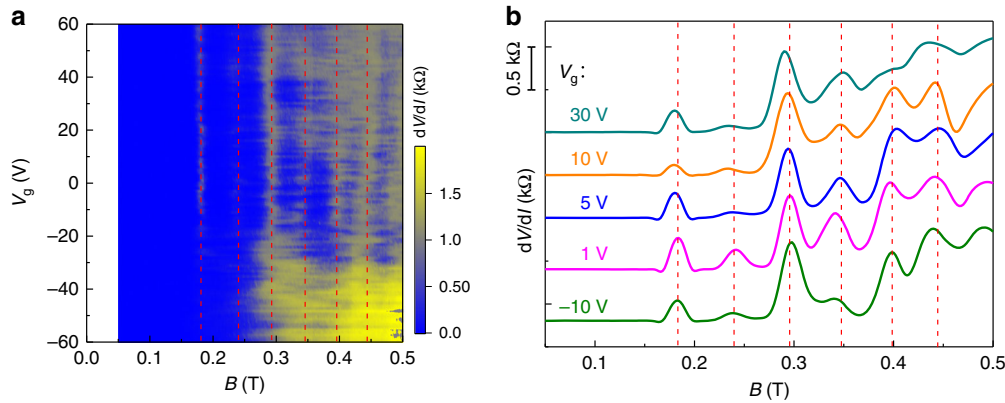


Fig. 4 The evolution of differential resistance with magnetic field **B** and V_g . **a** The dV/dI as a function of **B** and V_g with $I_{ac} = 1$ nA and without applying I_{dc} . The vertical dashed lines are eyes guided. **b** The cut lines of dV/dI as a function of **B** extracted from **a** at $V_g = 30, 10, 5, 1,$ and -10 V, respectively. The curves have been shifted for clarity. The dV/dI peaks emerge periodically with a period of $\Delta B = 0.055$ T.

In Dirac semimetal Cd_3As_2 , each Dirac cone splits into two Weyl cones along the direction of the magnetic field³⁹ (Supplementary Fig. 2). Because of the shift, the Andreev pair states will gain a finite center of mass momentum $\Delta k = \frac{g\mu_B B}{\hbar v_f}$, where g is the Landé factor, μ_B is the Bohr magneton, \hbar is the reduced Planck constant, and v_f is the Fermi velocity. The finite momentum results in a dephasing of the superconducting pairing potential and eventually modulates the critical current periodically in magnetic field^{27,28}. The oscillation period in magnetic field satisfies the relation $\Delta k \times L = \pi$. Using an averaged $g = 30$ as reported in literatures⁴⁰ and Fermi velocity $v_f = 5 \times 10^5 \text{ ms}^{-1}$ we obtain the expected period $\Delta B \sim 1.98$ T which is around 40 times larger than the measured period 0.05 T. This means the Zeeman effect is not likely to be the dominant cause of the supercurrent oscillations. Spin-orbit coupling (SOC) can also give rise to an anomalous momentum shift and thereby oscillatory patterns^{36,41}. However, the SOC-related momentum shift requires the field in-plane perpendicular to the current, which does not apply to our case.

If there is a small perpendicular component of the applied magnetic field due to misalignment, the conventional Fraunhofer diffraction pattern may come into effect⁴². The junctions on the same nanoplate should have similar Fraunhofer patterns and the oscillation period should be proportional to the $1/L$. However, Junction B ($L = 500$ nm) in the same nanoplate shows a longer oscillation period than that of Junction A ($L = 300$ nm) (Supplementary Fig. 3). Therefore, the effect of Fraunhofer diffraction pattern can be simply ruled out. To further exclude the effect of possible perpendicular field components, we have also studied the critical current oscillations under an in-plane magnetic field perpendicular to the current direction (Supplementary Fig. 4). With the increase of channel length L , the location of the first node shifts to lower magnetic field. Such a length dependence of critical current oscillations is consistent with the Fraunhofer diffraction pattern, while is sharply contrasted to that for a parallel magnetic field. Therefore, the contamination of perpendicular field components can be safely ruled out. In this way, the possible interference effects related to in-plane perpendicular fields, including SOC-induced momentum shift and SQUID-like interference, can also be easily excluded as the cause of supercurrent oscillations.

It has been reported that the in-plane orbital interference can also induce the critical current oscillations³⁴⁻³⁶. As illustrated in Fig. 5a, we can model the phase difference $\phi_1(x_1) - \phi_2(x_2)$ of the superconducting pairs, arising from the in-plane field orbital effect³⁵:

$$\phi_1(x_1) - \phi_2(x_2) = \frac{\pi \mathbf{B}(x_1 - x_2)t}{\Phi_0}, \quad (1)$$

where t is the thickness of nanoplate, and $\phi_1(x_1)$ and $\phi_2(x_2)$ are the phases of the order parameters of superconductors 1 and 2 at the position x_1 and x_2 , respectively, along the width of the junction. For a bulk pairing state, the trajectory traverses the whole bulk and the total integration of the accumulated phase gives a negligible net phase shift, which only results in a I_c decay without oscillations (Supplementary Fig. 5). For a surface pairing state, on the other hand, the trajectory will come along the circumferential direction of the flake. The surface related supercurrent can be expressed as³⁵:

$$I_c^{\text{surface}}(\Delta\phi, \mathbf{B}) = \int_{-\frac{W}{2}}^{\frac{W}{2}} \int_{-\frac{W}{2}}^{\frac{W}{2}} dx_1 dx_2 \frac{1}{r^\epsilon} \sin(\Delta\phi + \phi_1(x_1) - \phi_2(x_2)), \quad (2)$$

where W is the junction width, $r = \sqrt{L^2 + (x_1 - x_2)^2}$ is the distance between two point (x_1, x_2) , and ϵ denotes the phase coherent strength along the x direction (Supplementary Fig. 6). Considering the magnetic screening effect from superconducting electrodes (Supplementary Fig. 7), the devices experienced magnetic field is smaller than the applied field, which is denoted by $\alpha \mathbf{B}$ ($\alpha < 1$). The critical current is defined as the maxima in one period of 2π phase, $I_c(\mathbf{B}) = \max[I(\Delta\phi, \mathbf{B})]$. As shown in Fig. 5b, the oscillating I_c under high magnetic fields can be well fitted by the model of surface in-plane field orbital effect and the fitting results give the parameters $\epsilon = 0.22$ and $\alpha = 0.2$.

From the modeling and fitting results, we can conclude that the supercurrent is carried mainly by the surface states of the nanoplate under high magnetic field. The periodic critical current oscillations can be understood by considering the in-plane orbital effect. This work provides a flexible gate and magnetic field manipulations of Fermi-arc superconductivity. Compared with the finite momentum pairing observed in topological insulator³⁵, we would like to clarify the differences between our work and that in Bi_2Se_3 . First, Bi_2Se_3 and Cd_3As_2 belong to different topological phases, that is, Bi_2Se_3 is a strong topological insulator protected by the time-reversal symmetry, while Cd_3As_2 is a 3D Dirac semimetal with an extra C_4 rotational symmetry. In addition, the surface nature of the two systems is topologically different. The surface states of a Dirac semimetal are in the form of Fermi arcs, in stark contrast with the Fermi surface in topological insulator surface. As the Fermi arcs connect the surface projection points of the Weyl nodes, the density states of Fermi arcs can be tuned by tuning the bulk Fermi level. A maximum critical supercurrent is observed near Dirac point, which is totally different from the 2D Dirac systems of graphene and topological insulator surface. Especially, the Dirac semimetals transform into Weyl semimetals

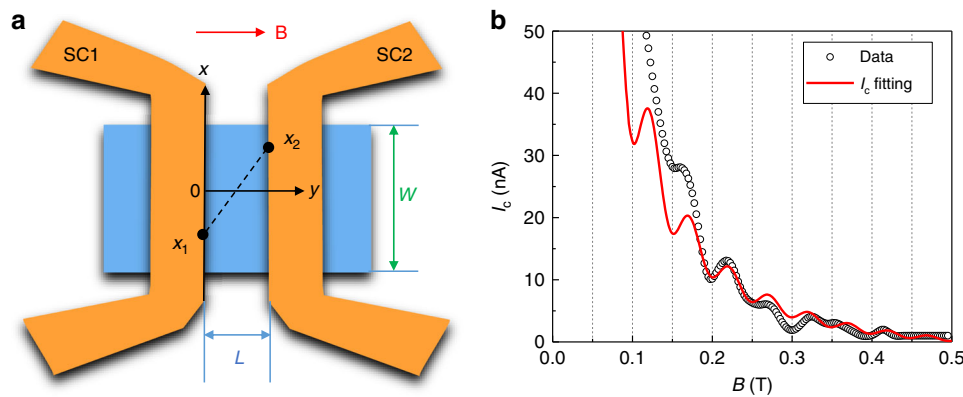


Fig. 5 Modeling Josephson interference in regime of in-plane field orbital effect. **a** Within two superconducting (SC) leads, pairing electrons traverse from position x_1 of SC1 to position x_2 of SC2, accumulating phase $\phi_2(x_2) - \phi_1(x_1)$. **b** The fit of I_c for $B > 70$ mT using the model of surface in-plane field orbital effect. The experimental data are from the $I_c(B)$ at $V_g = -10$ V.

as applying magnetic field to break the time-reversal symmetry. The Fermi arcs start to deform and chirality-related polarization arises (Supplementary Fig. 8), providing a good platform for the investigation of superconductivity of chiral polarized states.

Methods

Sample synthesis. High quality Cd_3As_2 nanoplates were synthesized by chemical vapor deposition method⁴³. Cd_3As_2 powders with high purity (>99.99%) were placed in the center of horizontal quartz tube. Silicon wafers with 5 nm gold thin film were placed downstream as substrates to collect the products. The quartz tube was first flushed three times with Argon gas to get out of oxygen, then gradually heated from room temperature to 700 °C within 20 min, and kept for 10 min at 700 °C along with an Argon gas flow of 20 s.c.c.m. The system was then cooled down naturally. The products of Cd_3As_2 nanoplates were collected on the silicon wafer substrates.

Device fabrication. Individual Cd_3As_2 nanoplate was transferred into silicon substrates with an oxide layer (SiO_2 , 285 nm). The nanoplate thickness t is about 80 nm. After a series process of standard e-beam lithography and Ar^+ plasma etching, Nb/Pd electrodes (100 nm/2 nm) were deposited in situ by sputtering.

Transport measurement. Transport measurements were performed in a dilution refrigerator (Oxford Instruments Triton 200) with a base temperature ~ 12 mK. With the use of standard lock-in technique (SR830) in the pseudo-four-probe current-voltage geometry, the electrical signals were acquired. The differential resistance (dV/dI) was measured by applying a small a.c bias current I_{ac} (typically in the range of 0.5–5 nA for different sweeping range) and concurrently measuring the a.c voltage. For the measurement of critical currents, a d.c bias signal I_{dc} was superimposed on the I_{ac} .

Data availability

The data that support the findings of this study are available from the corresponding author upon reasonable request.

Received: 24 August 2019; Accepted: 16 February 2020;

Published online: 02 March 2020

References

- Hasan, M. Z. & Kane, C. L. Colloquium: topological insulators. *Rev. Mod. Phys.* **82**, 3045–3067 (2010).
- Qi, X.-L. & Zhang, S.-C. Topological insulators and superconductors. *Rev. Mod. Phys.* **83**, 1057–1110 (2011).
- Bernevig, B. A. It's been a Weyl coming. *Nat. Phys.* **11**, 698–699 (2015).
- Armitage, N. P., Mele, E. J. & Vishwanath, A. Weyl and Dirac semimetals in three-dimensional solids. *Rev. Mod. Phys.* **90**, 015001 (2018).
- Wan, X., Turner, A. M., Vishwanath, A. & Savrasov, S. Y. Topological semimetal and fermi-arc surface states in the electronic structure of pyrochlore iridates. *Phys. Rev. B* **83**, 205101 (2011).
- Wang, Z., Weng, H., Wu, Q., Dai, X. & Fang, Z. Three-dimensional Dirac semimetal and quantum transport in Cd_3As_2 . *Phys. Rev. B* **88**, 125427 (2013).
- Xu, S. Y. et al. Observation of Fermi arc surface states in a topological metal. *Science* **347**, 294–298 (2015).
- Lv, B. Q. et al. Experimental discovery of Weyl semimetal TaAs. *Phys. Rev. X* **5**, 031013 (2015).
- Wang, L. X., Li, C. Z., Yu, D. P. & Liao, Z. M. Aharonov-Bohm oscillations in Dirac semimetal Cd_3As_2 nanowires. *Nat. Commun.* **7**, 10769 (2016).
- Lin, B.-C. et al. Gate-tuned Aharonov-Bohm interference of surface states in a quasiballistic Dirac semimetal nanowire. *Phys. Rev. B* **95**, 235436 (2017).
- Potter, A. C., Kimchi, I. & Vishwanath, A. Quantum oscillations from surface Fermi arcs in Weyl and Dirac semimetals. *Nat. Commun.* **5**, 5161 (2014).
- Moll, P. J. W. et al. Transport evidence for Fermi-arc-mediated chirality transfer in the Dirac semimetal Cd_3As_2 . *Nature* **535**, 266–270 (2016).
- Wang, C. M., Sun, H. P., Lu, H. Z. & Xie, X. C. 3D quantum Hall effect of Fermi arcs in topological semimetals. *Phys. Rev. Lett.* **119**, 136806 (2017).
- Schumann, T. et al. Observation of the quantum Hall effect in confined films of the three-dimensional Dirac semimetal Cd_3As_2 . *Phys. Rev. Lett.* **120**, 016801 (2018).
- Nishihaya, S. et al. Gate-tuned quantum Hall states in Dirac semimetal $(\text{Cd}_{1-x}\text{Zn}_x)_3\text{As}_2$. *Sci. Adv.* **4**, eaar5668 (2018).
- Zhang, C. et al. Quantum Hall effect based on Weyl orbits in Cd_3As_2 . *Nature* **565**, 331–336 (2019).
- Lin, B. C. et al. Observation of an odd-integer Quantum Hall effect from topological surface states in Cd_3As_2 . *Phys. Rev. Lett.* **122**, 036602 (2019).
- Wang, S., Lin, B.-C., Wang, A.-Q., Yu, D.-P. & Liao, Z.-M. Quantum transport in Dirac and Weyl semimetals: a review. *Adv. Phys.: X* **2**, 518–544 (2017).
- He, L. et al. Pressure-induced superconductivity in the three-dimensional topological Dirac semimetal Cd_3As_2 . *Npj Quantum Mater.* **1**, 16014 (2016).
- Wang, H. et al. Observation of superconductivity induced by a point contact on 3D Dirac semimetal Cd_3As_2 crystals. *Nat. Mater.* **15**, 38–42 (2016).
- Aggarwal, L. et al. Unconventional superconductivity at mesoscopic point contacts on the 3D Dirac semimetal Cd_3As_2 . *Nat. Mater.* **15**, 32–37 (2016).
- Li, C.-Z. et al. Bulk and surface states carried supercurrent in ballistic Nb-Dirac semimetal Cd_3As_2 nanowire-Nb junctions. *Phys. Rev. B* **97**, 115446 (2018).
- Yu, W. et al. π and 4π Josephson effects mediated by a Dirac semimetal. *Phys. Rev. Lett.* **120**, 177704 (2018).
- Wang, A. Q. et al. 4π -periodic supercurrent from surface states in Cd_3As_2 nanowire-based Josephson junctions. *Phys. Rev. Lett.* **121**, 237701 (2018).
- Li, C. Z. et al. Two-carrier transport induced hall anomaly and large tunable magnetoresistance in Dirac semimetal Cd_3As_2 nanoplates. *ACS Nano* **10**, 6020–6028 (2016).
- Crosser, M. S. et al. Nonequilibrium transport in mesoscopic multi-terminal SNS Josephson junctions. *Phys. Rev. B* **77**, 014528 (2008).
- Fulde, P. & Ferrell, R. A. Superconductivity in a strong spin-exchange field. *Phys. Rev.* **135**, A550–A564 (1964).
- Larkin, A. I. & Ovchinnikov, Y. N. Inhomogeneous state of superconductors. *Sov. Phys. JETP* **20**, 762–769 (1965).
- Demler, E. A., Arnold, G. B. & Beasley, M. R. Superconducting proximity effects in magnetic metals. *Phys. Rev. B* **55**, 15174–15182 (1997).
- Ryazanov, V. V. et al. Coupling of two superconductors through a ferromagnet: evidence for a π junction. *Phys. Rev. Lett.* **86**, 2427–2430 (2001).
- Blum, Y., Tsukernik, A., Karpovskii, M. & Palevski, A. Oscillations of the superconducting critical current in Nb-Cu-Ni-Cu-Nb junctions. *Phys. Rev. Lett.* **89**, 187004 (2002).
- Kontos, T. et al. Josephson junction through a thin ferromagnetic layer: negative coupling. *Phys. Rev. Lett.* **89**, 137007 (2002).

33. Murani, A. et al. Ballistic edge states in Bismuth nanowires revealed by SQUID interferometry. *Nat. Commun.* **8**, 15941 (2017).
34. Hart, S. et al. Controlled finite momentum pairing and spatially varying order parameter in proximitized HgTe quantum wells. *Nat. Phys.* **13**, 87–93 (2017).
35. Chen, A. Q. et al. Finite momentum Cooper pairing in three-dimensional topological insulator Josephson junctions. *Nat. Commun.* **9**, 3478 (2018).
36. Assouline, A. et al. Spin-Orbit induced phase-shift in Bi₂Se₃ Josephson Junctions. *Nat. Commun.* **10**, 126 (2019).
37. Li, C. et al. 4π -periodic Andreev bound states in a Dirac semimetal. *Nat. Mater.* **17**, 875–880 (2018).
38. Li, C. et al. Zeeman effect induced $0-\pi$ transitions in ballistic Dirac semimetal Josephson junctions. *Phys. Rev. Lett.* **123**, 026802 (2019).
39. Gorbar, E. V., Miransky, V. A. & Shovkovy, I. A. Engineering Weyl nodes in Dirac semimetals by a magnetic field. *Phys. Rev. B* **88**, 165105 (2013).
40. Jeon, S. et al. Landau quantization and quasiparticle interference in the three-dimensional Dirac semimetal Cd₃As₂. *Nat. Mater.* **13**, 851–856 (2014).
41. Buzdin, A. Direct coupling between magnetism and superconducting current in the Josephson φ_0 junction. *Phys. Rev. Lett.* **101**, 107005 (2008).
42. Veldhorst, M. et al. Josephson supercurrent through a topological insulator surface state. *Nat. Mater.* **11**, 417–421 (2012).
43. Li, C. Z. et al. Giant negative magnetoresistance induced by the chiral anomaly in individual Cd₃As₂ nanowires. *Nat. Commun.* **6**, 10137 (2015).

Acknowledgements

This work was supported by National Key Research and Development Program of China (Nos. 2018YFA0703703 and 2016YFA0300802), and NSFC (Nos. 91964201, 61825401, and 11774004).

Author contributions

Z.-M.L., C.L., and A.B. conceived and supervised this work. C.-Z.L., A.-Q.W., and C.L. fabricated the devices and performed the measurements. Z.-M.L., C.L., C.-Z.L., A.-Q.W., and A.B. analyzed the data and wrote the paper. D.-P.Y. contributed to the data analysis. W.-Z.Z. grew the nanoplates.

Competing interests

The authors declare no competing interests.

Additional information

Supplementary information is available for this paper at <https://doi.org/10.1038/s41467-020-15010-8>.

Correspondence and requests for materials should be addressed to C.L. or Z.-M.L.

Peer review information *Nature Communications* thanks the anonymous reviewer(s) for their contribution to the peer review of this work.

Reprints and permission information is available at <http://www.nature.com/reprints>

Publisher's note Springer Nature remains neutral with regard to jurisdictional claims in published maps and institutional affiliations.



Open Access This article is licensed under a Creative Commons Attribution 4.0 International License, which permits use, sharing, adaptation, distribution and reproduction in any medium or format, as long as you give appropriate credit to the original author(s) and the source, provide a link to the Creative Commons license, and indicate if changes were made. The images or other third party material in this article are included in the article's Creative Commons license, unless indicated otherwise in a credit line to the material. If material is not included in the article's Creative Commons license and your intended use is not permitted by statutory regulation or exceeds the permitted use, you will need to obtain permission directly from the copyright holder. To view a copy of this license, visit <http://creativecommons.org/licenses/by/4.0/>.

© The Author(s) 2020